

DIGITAL ACCESS TO SCHOLARSHIP AT HARVARD
DASH.HARVARD.EDU

HARVARD LIBRARY


Monitoring vegetation phenology using an infrared-enabled security camera

Citation

Petach, Anika R., Michael Toomey, Donald M. Aubrecht, and Andrew D. Richardson. 2014. "Monitoring Vegetation Phenology Using an Infrared-Enabled Security Camera." Agricultural and Forest Meteorology 195-196 (September): 143–151.

Published version

https://doi.org/10.1016/j.agrformet.2014.05.008

Link

http://nrs.harvard.edu/urn-3:HUL.InstRepos:12748552

Terms of use

This article was downloaded from Harvard University's DASH repository, and is made available under the terms and conditions applicable to Open Access Policy Articles (OAP), as set forth at https://harvardwiki.atlassian.net/wiki/external/NGY5NDE4ZjgzNTc5NDQzMGIzZWZhMGFlOWI2M2EwYTg

Accessibility

https://accessibility.huit.harvard.edu/digital-accessibility-policy

Share Your Story

The Harvard community has made this article openly available.
Please share how this access benefits you. Submit a story

Monitoring vegetation phenology using an infrared-enabled security camera

Anika R. Petach[1], Michael Toomey[2], Donald M. Aubrecht[2], and Andrew D. Richardson[2,*]

[1]Harvard University, Department of Earth and Planetary Sciences and School of Engineering and Applied Sciences
[2]Harvard University, Department of Organismic and Evolutionary Biology

*HUH, 22 Divinity Avenue, Cambridge, MA 02138; arichardson@oeb.harvard.edu.

Abstract

Sensor-based monitoring of vegetation phenology is being widely used to quantify phenological responses to climate variability and change. Digital repeat photography, in particular, can characterize the seasonality of canopy greenness. However, these data cannot be directly compared to satellite vegetation indices (e.g., NDVI, the normalized difference vegetation index) that require information about vegetation properties at near-infrared (NIR) wavelengths. Here, we develop a new method, using an inexpensive, NIR-enabled camera originally designed for security monitoring, to calculate a "camera NDVI" from sequential visible and visible+NIR photographs. We use a lab experiment for proof-of-concept, and then test the method using a year of data from an ongoing field campaign in a mixed temperate forest. Our analysis shows that the seasonal cycle of camera NDVI is almost identical to that of NDVI measured using narrow-band radiometric instruments, or as observed from space by the MODIS platform. This camera NDVI thus provides different information about the state of the canopy than can be obtained using only visible-wavelength imagery. In addition to phenological monitoring, our method should be useful for a variety of applications, including continuous monitoring of plant stress and quantifying vegetation responses to manipulative treatments in large field experiments.

Keywords: Digital repeat photography; green chromatic coordinate (g_{CC}); near-surface remote sensing; normalized difference vegetation index (NDVI); phenology; stress monitoring.

Introduction

The phenology of terrestrial vegetation is highly sensitive to climate variability and change (Rosenzweig et al., 2007; Migliavacca et al., 2012). In the context of climate change, phenology is important because it mediates many of the feedbacks between terrestrial vegetation and the climate system (Richardson et al., 2013a). From an ecological perspective, phenology plays an important role in both competitive interactions and trophic dynamics, as well as in reproductive biology, primary production, and nutrient cycling (Morisette et al., 2009).

Satellite remote sensing can provide global coverage of vegetation phenology, but suffers from tradeoffs between spatial and temporal resolution (Zhang et al., 2003; White et al., 2009). Thus, over the last decade, there has been great enthusiasm for increased on-the-ground monitoring of phenology (Betancourt et al., 2005; Morisette et al., 2009; Polgar and Primack, 2011). The general objective of these efforts is to better understand spatial and temporal variation in phenology, and how this variability is driven by environmental factors such as temperature, precipitation, and photoperiod (or insolation). Citizen science networks, such as the USA National Phenology Network (http://www.usanpn.org) and Project Budburst (http://budburst.org), are playing an important role in this monitoring, by engaging large numbers of motivated volunteers and establishing standardized protocols.

Instrument-based approaches (Richardson et al., 2013b) provide a compelling alternative to observer-based phenology, because of the potential for high frequency, automated data collection in a manner that is scalable for regional or continental monitoring. In this context, digital repeat photography (e.g. Richardson et al., 2007, 2009; Sonnentag et al., 2012) is an attractive option because images can be analyzed either qualitatively or quantitatively, and analysis can focus on individual organisms or integrate across the field of view to obtain a community- or canopy-level perspective. Compared to data collected by a human observer, which tend to focus on discrete phenophases, such as flowering or budburst, the entire seasonal trajectory of canopy greenness can be characterized from digital camera imagery. Additionally, the archived images provide a permanent visual record that can be reanalyzed as new tools and questions are developed. Camera-based monitoring (e.g. the PhenoCam network, http://phenocam.sr.unh.edu/) thus provides data at a spatial scale that is intermediate between ground observations of individual plants and satellite remote sensing.

To date, most camera-based monitoring of vegetation phenology has been conducted using standard, consumer-grade digital cameras (e.g. Sonnentag et al., 2012). These typically record a three-layer image (red, green and blue: RGB), which is sufficient for the representation of colors in the visible spectrum (VIS, λ = 400-700 nm) as perceived by the human eye. For quantitative analysis, the average value of each color layer for all pixels within a user-defined region of interest (ROI) is extracted from each image to yield a digital number triplet (R_{DN}, G_{DN}, B_{DN}). Then seasonal variation in the state of the canopy is characterized by the use of several color indices, such as the green chromatic coordinate ($g_{CC,}$, Eq. 1a) and excess green (G_{ex}, Eq. 1b) (Sonnentag et al., 2012; Richardson et al., 2013b):

$$g_{CC} = G_{DN}/(R_{DN} + G_{DN} + B_{DN}) \quad \text{Eq. 1a}$$

$$G_{EX} = 2G_{DN} - (R_{DN} + B_{DN}) \quad \text{Eq. 1b}$$

Conversely, satellite remote sensing of vegetation has traditionally used both visible and near-infrared (NIR, λ = 700-1400 nm) wavelengths. The reason for this is that healthy vegetation can be distinguished from other land cover types by its unique spectral signature, which combines low reflectance in the VIS with high reflectance in the NIR. Thus, the camera indices presented above, which are based only VIS wavelengths, are not directly comparable to standard satellite vegetation indices such as NDVI (Normalized Difference Vegetation Index, Eq. 1c), calculated from red band and NIR band reflectances (ρ_R and ρ_{NIR}, respectively) (Tucker, 1979).

$$NDVI = (\rho_R - \rho_{NIR})/(\rho_R + \rho_{NIR}) \quad \text{Eq. 1c}$$

Intriguingly, the CCD (charge-coupled device) or CMOS (complementary metal-oxide-semiconductor) imaging sensors used in most digital cameras are sensitive to wavelengths in the NIR portion of the spectrum. An infrared cut filter is typically used to block these wavelengths from reaching the imaging sensor, as they are beyond the spectral range to which the human eye is sensitive and are thus not necessary for conventional color photography. Customized cameras have been used in the past to leverage this NIR sensitivity (Shibayama et al., 2009, 2011; Sakamoto et al., 2010, 2012; Nijland et al., 2013). For example, using a two-camera system Sakamoto et al. (2012) calculated an NDVI-style index that was more akin to the conventional NDVI than either g_{CC} or G_{EX}. The two-camera approach allows for simultaneous recording of information about the VIS and NIR properties of vegetation, but creates challenges related to camera alignment, cross-calibration, and synchronization of image capture. Very recently, relatively low-cost NDVI cameras have become available (e.g. MaxMax, Event-38, and Regent

brands), but these have not been produced with long-term monitoring in mind, and such cameras are unable to also produce conventional RGB imagery—that is, infrared wavelengths are recorded at the expense of information in one of the RGB channels.

Here, we show that a commercially-available, network-enabled camera ("webcam") with a software-controlled infrared cut filter overcomes the above limitations. With the cut filter in place, standard 3-layer RGB imagery is recorded; with the filter removed, a monochrome RGB+NIR image is obtained. We develop a method to compute an NDVI-style vegetation index, which we call "camera NDVI", from this imagery. A lab experiment, conducted under controlled conditions, is used as a proof-of-concept. We then apply the method to a one-year archive of images from the Harvard Forest to demonstrate the feasibility of employ this method for field monitoring of vegetation phenology, where day-to-day variation in weather and lighting cause additional challenges. As a final test, we compare the seasonality of camera NDVI from the Harvard Forest data with that obtained using co-located narrow-band radiometric instruments and from satellite sensors. Data from our camera system will be of value for quality assessment of phenology products derived from satellite imagery (e.g. White et al., 2009).

Material and Methods

Camera

We used a NetCam SC IR (StarDot Technologies, Buena Park, CA) camera, featuring a Micron ½" CMOS active-pixel digital imaging sensor and configured for 1.3 megapixel (1296 x 976) output. The camera was set at manual (fixed) white balance and, unless otherwise noted, automatic exposure. With a built-in uClinux operating system, the camera operates as a standalone system with Internet connectivity. Command scripts running on the camera controlled the infrared cut filter, image capture, and image upload to a remote server via FTP. The customized scripts used here are available in the "Tools" section of the PhenoCam project page (http://phenocam.sr.unh.edu/webcam/tools/) or from the corresponding author.

Proof-of-concept lab experiment

We conducted a lab experiment to evaluate whether camera imagery can be used to accurately characterize the broadband spectral properties of different materials. We used the StarDot camera to record sequential color RGB and monochrome RGB+NIR images of materials

with a wide range of spectral signatures (Figure 1). Each sample was illuminated from above with a 50 W Halogen lamp designed for indoor diffuse reflectance measurements (ASD ProLamp, Analytical Spectral Devices Inc., Boulder, CO). The StarDot camera was mounted on a tripod to the side of the sample and inclined downward at an angle of about 45°. Each sample filled approximately one-quarter of the camera's field of view. For quality assurance, we included a multi-color reference panel in each image, made by painting red, green, blue, white and grey strips on a flat piece of plastic. We recorded four images of each sample: one image at fixed exposure (1/300 s) for both color RGB and monochrome RGB+NIR images, and one image at automatic exposure for both color RGB and monochrome RGB+NIR. Automatic exposure values were determined by the camera. The mean automatic exposure for the color RGB images was 1/30 s (minimum 1/120 s), compared with 1/200 s (minimum 1/350 s) for the monochrome RGB+NIR images. Thus the fixed exposure images were almost always under-exposed compared to the automatic exposure images.

We measured the reflectance spectrum (λ = 350–2500 nm) of each sample using a spectroradiometer (ASD FieldSpec 3, Analytical Spectral Devices Inc.) connected to a 5 cm (2 inch) three-port integrating sphere (SphereOptics, Concord, NH) and a 10 W hemispheric collimated light source with a 6 V regulated power supply. White Spectralon discs were used as reference standards. The sphere featured an 8° near-normal incidence port, such that reflectance measurements include both diffuse and specular components. We processed the raw data to reflectances (1 nm increment) using ViewSpecPro software (Analytical Spectral Devices Inc.). Spectroradiometer NDVI was calculated using red and NIR band reflectances; specific wavelength ranges are reported below.

Most of the samples (42) for this experiment were leaves picked from a selection of trees and shrubs native to New England, representing a wide range of leaf health and corresponding colors, from fresh dark green to senesced red to fallen brown leaves (Figure 1). We included other materials, including asphalt, cardboard, wood, and several paint color chips, for a total of 51 samples.

Field data

We used field data from an ongoing measurement campaign at the 40 m "Barn Tower" (42.5353°N 72.1899°W) at the Harvard Forest, near the town of Petersham, MA, 110 km west of

Boston. Mixed forest stands surrounding the tower are dominated by the deciduous species red oak (*Quercus rubra* L., ~40% of basal area) and red maple (*Acer rubrum* L., ~20% of basal area), with evergreen white pine (*Pinus strobus* L.) the dominant conifer. The MODIS land cover classification for the tower, and the land immediately surrounding the tower, is deciduous broadleaf forest.

We used imagery (April 1, 2012 through March 30, 2013) from a StarDot camera that is mounted at the top of the tower. The camera points north and is inclined ~30° below horizontal. As in the lab experiments, command scripts on the camera trigger the infrared cut filter and obtain successive (about 30 s apart) color RGB and monochrome RGB+NIR imagery. Automatic exposure is used for each image. Images are uploaded by FTP to a remote server every 15 minutes between 4 a.m. and 10 p.m.

Also mounted atop the same tower is a pair of 4-channel (blue: 470 ± 20 nm, green: 557 ± 25 nm, red: 605 ± 35 nm, NIR: 750 ± 42 nm) narrowband radiometric sensors (Model 1850, Skye Instruments, Llandrindod Wells, UK). One unit with a cosine diffuser is pointed upwards to measure incident solar radiation, while the second unit, with a 25° field of view, is pointed in the same direction as the StarDot camera to measure radiation reflected by the canopy. We log measurements every 15 seconds and record 30 minute averages on a datalogger (CR1000, Campbell Scientific, Logan, UT). From these data, we calculated canopy reflectance (ρ_i) as in Eq. 2, where $Q_i\downarrow$ and $Q_i\uparrow$ are measurements of the incident and reflected quantum flux, respectively, for each band i, and the calibration constant (k_i) determined under natural (sunlit) conditions using a Spectralon panel.

$$\rho_i = k_i\left(Q_i^{\uparrow}/Q_i^{\downarrow}\right) \qquad \text{Eq. 2}$$

We calculated two indices from the narrowband radiometric sensors: radiometer NDVI (Eq. 3a) and radiometer g_{CC} (Eq. 3b):

$$\text{radiometer NDVI} = (\rho_{750} - \rho_{605})/(\rho_{750} + \rho_{605}) \qquad \text{Eq. 3a}$$

$$\text{radiometer } g_{CC} = \rho_{557}/(\rho_{605} + \rho_{557} + \rho_{470}) \qquad \text{Eq. 3b}$$

Image processing

Briefly, image analysis for both lab and field data included manual delineation of an appropriate ROI and extraction of color channel information for that ROI in each image. We also

used an optical character recognition algorithm to read the image exposure from the text overlay at the top of each image.

For the lab experiment, the ROI was adjusted for each sample to include as much of the sample as possible. For the field data, we defined separate deciduous (predominantly red oak and red maple) and conifer (white pine) ROIs, which were each roughly 440 x 440 pixels in size. The camera field of view did not change over time, and thus these ROIs were fixed over the period of analysis.

We processed the camera imagery as follows. For each sample, we defined the ROI and determined the average pixel value (digital number) across the ROI for three channels in the color RGB images (R_{DN}, G_{DN}, B_{DN}) and one channel in the monochromatic RGB+IR images (Z_{DN}). If both images were taken at the same exposure, then the monochrome RGB+IR images could be partitioned to a visible component (Y_{DN}) plus a NIR component (X_{DN}) according to Eq. 4a, with the visible component calculated from the color RGB images as in Eq. 4b (Daniel Lawton, StarDot Technologies, personal communication). Then the NIR component, X_{DN}, was estimated as $Z_{DN} - Y_{DN}$.

$$Z_{DN} = Y_{DN} + X_{DN} \quad \text{Eq. 4a}$$

$$Y_{DN} = 0.30 * R_{DN} + 0.59 * G_{DN} + 0.11 * B_{DN} \quad \text{Eq. 4b}$$

However, if the images were taken at different exposures (where E_Y denotes the exposure of the color RGB image and E_Z the exposure of the RGB+IR image), then these exposure differences had to be accounted for. Exploratory analyses indicated that division through by the square root of the exposure time offered a straightforward solution (Eq. 5a-d) to exposure adjustment. Note that camera systems with different gamma values, where γ is the exponent in the power law relationship between input and output signals of digital imaging systems, may be different (cf. Sakamoto et al., 2010, 2012). Taking the square root of E assumes a γ = 2.0, a reasonable approximation of the actual StarDot value of γ = 1.7 (Daniel Lawton, StarDot Technologies, personal communication). However, our results were essentially the same regardless of whether we used 2.0 or 1.7.

$$Z'_{DN} = Z_{DN}/\sqrt{E_Z} \quad \text{Eq. 5a}$$

$$R'_{DN} = R_{DN}/\sqrt{E_Y} \quad \text{Eq. 5b}$$

$$Y'_{DN} = Y_{DN}/\sqrt{E_Y} \quad \text{Eq. 5c}$$

$$X'_{\mathrm{DN}} = Z'_{\mathrm{DN}} - Y'_{\mathrm{DN}} \qquad \text{Eq. 5d}$$

We calculated camera NDVI as in Eq. 6, in terms of exposure-adjusted digital numbers. For fixed-exposure images, the same calculation was used, ignoring the primes (′).

$$\text{Camera NDVI} = \left(X'_{\mathrm{DN}} - R'_{\mathrm{DN}}\right)/\left(X'_{\mathrm{DN}} + R'_{\mathrm{DN}}\right) \qquad \text{Eq. 6}$$

For both radiometer and camera data, there was substantial variability in the derived indices at the 30 minute time step, which may be associated with factors such as overall light levels, cloudiness, and illumination geometry (see further analysis in Results). After comparing various averaging, quantile, and filtering methods, we derived daily estimates by calculating the arithmetic mean across all observations where the incident photosynthetic photon flux density (PPFD; measured at the top of the tower using a PQS-1 quantum sensor, Kipp & Zonen, Delft, the Netherlands) was greater than 200 μmol m^{-2} s^{-1}. This method reduced day-to-day variability in the resulting time series better than the 90th percentile approach used by Sonnentag et al. (2012), although an obvious advantage of the latter approach is that it does not require solar radiation data.

Because R'_{DN} and X'_{DN} are not direct measurements of reflectance, the magnitude of camera NDVI depends on the spectral distribution of the incident light. Thus, camera NDVI values from the lab experiments are not directly comparable to those from the field experiment, and those from the field experiment are not comparable to either radiometer or satellite NDVI values. To compensate for this, we re-scaled camera NDVI (yielding camera NDVI^{R}) by estimating the coefficients of a linear regression between camera NDVI (for the deciduous ROI) and radiometer NDVI, where a is a slope coefficient, b is the y-axis intercept and ε is the model residual:

$$\text{radiometer NDVI} = a(\text{camera NDVI}) + b + \varepsilon \qquad \text{Eq. 7}$$

Results

Lab experiment

Spectral reflectance signatures differ markedly among the 51 samples scanned by the spectroradiometer (Figure 1). There are pronounced differences in reflectance spectra between green, yellowing, and red leaves, but the non-foliar samples added greatly to the variability among samples across both visible and near-infrared wavelengths. The variation in reflectance

across samples is smallest for violet and blue (400-500 nm) wavelengths, and largest for red (620-700 nm) and near infrared (700-1000 nm) wavelengths.

For the fixed exposure imagery (results not illustrated), digital numbers extracted from camera imagery for the red channel (R_{DN}) are well correlated with mean reflectance over red wavelengths (620-700 nm) measured with the spectroradiometer ($r = 0.91$). Similarly, digital numbers for the near infrared (X_{DN}) component of the RGB+NIR imagery are well correlated with mean reflectance over NIR wavelengths (700-1000 nm) measured with the spectroradiometer ($r = 0.87$). Camera NDVI is well correlated with spectroradiometer NDVI using these broad bands ($r = 0.91$), or using the spectral range of MODIS bands (band 1 = 620–670 nm, band 2 = 841–867 nm) ($r = 0.93$).

We used an iterative procedure to identify the wavelengths across which reflectance measured by the spectroradiometer is most highly correlated with R_{DN} and X_{DN} from the fixed exposure imagery. For R_{DN}, we obtained a correlation of $r = 0.96$ across the range from 570-660 nm (Figure 2A), whereas for X_{DN}, we find a correlation of $r = 0.91$ across the range from 805-815 nm (Figure 2B). For the fixed exposure imagery, there is an excellent correlation ($r = 0.99$) between camera NDVI and spectroradiometer NDVI calculated using these particular bands (Figure 2C).

We conducted a similar analysis for the automatic exposure imagery. Exposure-adjusted digital numbers (Eq. 5b, 5d) for each channel are best correlated with mean reflectance, measured by the spectroradiometer, across an appropriate range of wavelengths (Figure 3). For example, B'_{DN} is most strongly correlated with mean reflectance across violet and blue wavelengths (430-515 nm, $r = 0.92$), G'_{DN} with green wavelengths (510-570 nm, $r = 0.94$), R'_{DN} with yellow and red wavelength (575-710 nm, $r = 0.96$; Figure 4A), and X'_{DN} with near infrared wavelengths (800-815 nm, $r = 0.88$; Figure 4B). The contour plots in Figure 3 show how the strength of these correlations tended to fall off rapidly outside the optimal range. For example, R'_{DN} is not well correlated with wavelengths < 575 nm or >710 nm, and X'_{DN} is not well correlated with wavelengths < 700 nm. For the automatic exposure imagery, camera NDVI is very well correlated with spectroradiometer NDVI using either the most-highly-correlated bands identified here (i.e. red 575-710 nm and NIR 800-815 nm; $r = 0.96$, Figure 4C), or the standard MODIS bands ($r = 0.94$).

Results from the lab experiment demonstrate the potential of the StarDot camera imagery for characterizing the spectral properties of diverse materials, particularly in red and near infrared bands. By processing sequential VIS and VIS+NIR images, we are able to back-calculate the NIR component. Furthermore, this experiment shows that camera NDVI is strongly correlated with spectroradiometer NDVI when using either fixed exposure or automatic exposure imagery. Since field images are recorded with automatic exposures to optimize dynamic range under varying illumination conditions, our ability to correct for variations in exposure is critical. These lab results prove that camera NDVI is sensitive to the variation in reflectances of a wide range of materials and surfaces. This indicates the potential for monitoring canopy phenology in the field using a similar approach to characterize the seasonal variation in canopy optical properties, as described in the following section.

Field measurements

The green chromatic coordinate calculated from the narrowband radiometric sensors, radiometer g_{CC} (Figure 5A), exhibits a seasonal pattern that is typical of deciduous forests (e.g., Sonnentag et al., 2012; Richardson et al., 2013b). Radiometer g_{CC} rises rapidly in spring with budburst (day 115-120) and leaf development to a pronounced spiky peak (day 140; see Keenan et al., 2014, for discussion), before decreasing gradually over the course of the summer, and then declining rapidly (day 250) in autumn with leaf coloration and abscission (day 300). For the deciduous ROI, camera g_{CC} (Figure 5B) follows essentially the same seasonal pattern, with the notable exception of a more pronounced dip in greenness around day 290, corresponding to the peak of autumn colors and a marked increase in canopy redness that is clearly visible in the RGB camera imagery. The coniferous ROI shows a seasonally varying signal in camera g_{CC} (Figure 5C), but with substantially smaller amplitude than that for the deciduous ROI, reflecting the year-round presence of foliage but nevertheless indicating seasonal variation in foliar chlorophyll concentrations (Richardson et al., 2009). The start of spring green-up also begins about 30 days earlier, and the end of the autumn decline ends about 60 days later, for the coniferous ROI compared to the deciduous ROI.

By contrast, the seasonal cycle of radiometer NDVI differs from that of radiometer (or camera) g_{CC} (Figure 5D). The primary difference is the absence of the spike seen in g_{CC} around day 140. A secondary difference is the presence of a broad plateau in radiometer NDVI from

about day 130 to day 240. As a result, radiometer NDVI gives a better representation of the seasonal dynamics of canopy leaf area index (LAI) than does radiometer g_{CC} (e.g. compare with Fig. 1 in Richardson et al., 2012). Additionally, the seasonal cycle of radiometer NDVI roughly parallels (and is comparable in magnitude to) that of MODIS NDVI (Figure 5D). In particular, the timing of the spring increase and autumn decrease in NDVI is similar in both time series. However, during the winter months the MODIS data are somewhat noisier than the radiometer data.

There is a strong linear relationship ($R^2 = 0.89$) between radiometer NDVI and camera NDVI for the deciduous ROI. The best-fit linear scaling coefficients (Eq. 7) are $a = 0.53 \pm 0.02$ SE and $b = 0.84 \pm 0.01$, with $\sigma(\varepsilon) = 0.041$. Henceforth, we focus on the rescaled time series, camera $NDVI^R$, for which the seasonal cycle is much more similar in shape to that of radiometer NDVI than camera g_{CC}. For example, the relative rate of increase in both radiometer NDVI and camera $NDVI^R$ for the deciduous region of interest in spring is more gradual than the corresponding rate of increase in radiometer or camera g_{CC}, and conspicuously absent in the camera $NDVI^R$ data for the deciduous region of interest is the g_{CC} spike that occurs around day 140. For the coniferous region of interest, camera g_{CC} shows a seasonal pattern that is less pronounced than that for the deciduous region of interest. However, there is no clear seasonal cycle in the camera $NDVI^R$ data for the coniferous region of interest. Together, these results suggest that camera NDVI is capturing different aspects of seasonal canopy dynamics than indices, such as g_{CC}, that are based only on visible wavelengths (cf. Nijland et al. 2013). The use of both g_{CC} and camera NDVI together give more information than can be obtained from either index on its own. The advantage of g_{CC} is that it is sensitive to leaf color, which is related to pigmentation (Keenan et al. 2014), while camera NDVI is a better proxy for LAI.

Non-phenological sources of variability in camera NDVI

Even with averaging of 30-minute data to a daily product, the signal-to-noise ratio of camera $NDVI^R$ is somewhat higher than that of camera g_{CC} (day-to-day variability being equal to about 8% of the seasonal amplitude for camera $NDVI^R$, compared with 5% for camera g_{CC}; compare Figures 5B and 5E), and indeed also higher than that of radiometer NDVI (compare figures 5E and 5D). Of course, some of the variation in both camera NDVI and radiometer NDVI can potentially be attributed to sky condition, shadow fraction, and illumination geometry, all of

which can change over the course of the day or between one day and the next. And, some of this variability is undoubtedly the result of the brief (30 s) lag between the VIS and VIS+NIR imagery, which is unavoidable as the camera needs some time to adjust after the cut filter has been triggered on or off.

We further investigate some of the factors associated with variability in camera $NDVI^R$ using the 30-minute data, focusing on the period from day 160 to day 200, when camera $NDVI^R$ for the deciduous region of interest is essentially stable at its maximum summertime value. During this period, camera $NDVI^R$ at the 30-minute time step (1 SD = 0.13) was 10 times more variable than at the daily time step (1 SD = 0.01). Much of the variability in the 30-minute data results from imagery captured under low-to-intermediate light levels (1 SD = 0.17 for PPFD < 500 μmol m^{-2} s^{-1}; 1 SD = 0.06 for PPFD ≥ 500 μmol m^{-2} s^{-1}). At both dawn and dusk, camera $NDVI^R$ is considerably lower, and markedly more variable, than at mid-day, indicating both a systematic bias and a lower signal-to-noise ratio under low-light conditions. However, excluding periods with PPFD < 200 μmol m^{-2} s^{-1}, the diurnal pattern (data from 6 a.m. to 6 p.m.) in camera $NDVI^R$ is negligible: a polynomial function of time of day accounts for no more than 2% of the total variance in camera $NDVI^R$. This suggests that illumination geometry has only a minimal effect on camera $NDVI^R$. Similarly, although camera $NDVI^R$ is highly variable when the ratio of diffuse/total PPFD is ≥ 0.90, the noisy observations are all associated with PPFD < 500 μmol m^{-2} s^{-1}.

A final—and important, because it can not be entirely eliminated by filtering for lower-light conditions—source of variation in camera $NDVI^R$ is the ratio of the exposure times for the RGB and RGB+NIR imagery, i.e. $E_{ratio} = E_Y/E_Z$. A second-order polynomial of E_{ratio} explains 73% of the variation in 30-minute camera $NDVI^R$, with both low (< 2) and high (>5) values of E_{ratio} contributing to this pattern. Filtering for periods with PPFD ≥ 500 μmol m^{-2} s^{-1} eliminates most instances of low E_{ratio}. High values of E_{ratio} are most often associated with anomalously long RGB exposures (high E_Y). The RGB images associated with these long exposures are characterized by an anomalously bluish cast. We are unable to identify the specific lighting conditions (total PPFD, PPFD variance, direct PPFD, diffuse PPFD, or the direct/total PPFD ratio) that cause this effect. However, even considering only data acquired with $2 < E_{ratio} < 5$, E_{ratio} still accounts for 40% of the variation in camera $NDVI^R$ between day 160 and day 200. Using a fixed exposure setting (with potentially different values of E_Y and E_Z), and limiting the

analysis to high-light, mid-day conditions, it should be possible to eliminate this source of variability in camera $NDVI^R$.

Discussion

We have proposed a method by which an off-the-shelf networked digital camera, originally marketed for security monitoring applications, can be repurposed and used to obtain information about the spectral properties of vegetation in both visible and NIR wavelengths, and thus to calculate NDVI-style indices (cf. Nijland et al. 2013, who found that imagery from a filtered, infrared-sensitive camera was of no more value than conventional RGB imagery for tracking plant phenology and health). The lab experiment described here is used as a proof-of-concept (Figs. 2, 4), and shows that not only can we back out the IR component from the RGB+NIR imagery, but also that our method for exposure-correction of auto-exposed imagery is effective. The field data, on the other hand, show how this method can be applied for long term monitoring of vegetation phenology in real-world conditions with varying solar illumination and weather conditions. Specifically, we show good agreement between data obtained using the camera NDVI method and the seasonal trajectory of NDVI measured using radiometric sensors (Fig. 5). This approach is highly economical: the camera used here retails for about US$1200, which is a fraction of the cost of a pair (upward- and downward-looking) of multi-channel radiometric sensors. While we did not rely on a reference panel for standardization, inclusion of a grey Spectralon (or other diffuse reflector) panel within the field of view of the camera would potentially be of value for normalization under changing illumination conditions (e.g. cloudy vs. sunny days); however, the results shown here suggest that even without this kind of calibration standard, it is possible to obtain high-quality data on the seasonal variation in canopy NDVI. Although our field experiment was conducted in a mixed forest ecosystem, there is no reason to believe that this method would not be applicable in other vegetation types, especially those with a strong seasonal cycle such as crops or grasslands. The signal-to-noise ratio may, however, be inadequate for tracking the seasonality of evergreen vegetation with a high LAI. This method is currently implemented at more than 40 core sites within the PhenoCam network (http://phenocam.sr.unh.edu), and future analysis of those data will confirm the viability of this approach.

Networked cameras are well suited to field monitoring applications because with Internet connectivity (using cell phone modems, this is now possible even at remote field sites) images can be archived to an off-site server, and camera functionality can be monitored remotely. Furthermore, since this eliminates the need for manually swapping out memory cards, the potential for shifts in camera alignment are minimized, making it is easier to maintain a constant field of view. This facilitates image processing and improves data quality.

We acknowledge that cameras with red and NIR sensitivity, primarily designed for precision agriculture applications, have been developed and are commercially available (e.g. the Agricultural Digital Camera by Tetracam, Inc., Chatsworth, CA, which retails for US$4800). These have been used for ecological studies (e.g. Steltzer and Welker, 2006; Higgins et al., 2011), but we are not aware of this type of camera being installed in the field for continuous, long-term monitoring applications. Conventional digital cameras have also been customized and used for similar work, but these have typically made use of two-camera systems, with one camera filtered for visible wavelengths and the other for near infrared wavelengths (e.g. Shibayama et al., 2009, 2011; Sakamoto et al., 2010, 2012; see also Nijland et al., 2013). What is unique about the present approach is that by controlling the camera's infrared cut filter we instead obtained sequential images from a single sensor, rather than simultaneous images from two sensors. Not only does the single-camera approach reduce costs, it also eliminates issues related to parallax, sensor calibration, and image alignment. Our method could, in principle, be used with other camera systems although the linear scaling coefficients (a, b) reported here are probably specific to the StarDot NetCam SC IR.

Compared to other low-cost, sensor-based methods for monitoring seasonal changes in the spectral properties of vegetation (e.g. radiometric instruments based on photodiodes, Garrity et al., 2010, or light emitting diodes, Ryu et al., 2010), a clear advantage of the camera approach is that it yields high-resolution images. This enables tracking the phenology of different organisms or groups of organisms by breaking the image into different regions of interest—e.g., deciduous and coniferous trees (e.g. Fig. 5E,F). False-color images similar to those traditionally generated from satellite imagery can also be generated using near infrared, red, and green bands (i.e. XRG rather than RGB), as shown in Figure 6. Thus, the camera effectively becomes a four-channel imaging sensor. We acknowledge that higher-quality spectral image data could, potentially, be obtained from existing, commercially available multichannel or hyper-spectral

cameras, e.g. Surface Optics SOC-710 or TetraCam MCA. However, for budget-limited observational and experimental studies, the system proposed here may represent an acceptable compromise, given its substantially lower cost and proven performance.

Our camera NDVI approach is conceptually similar to that used to obtain broadband NDVI from readily available radiometric measurements of incident and canopy-reflected visible (PPFD) and total shortwave radiation (Huemmrich et al., 1999; Wang et al., 2004; Jenkins et al., 2007; see review in Richardson et al., 2013b). The similarity of camera NDVI to radiometer NDVI, and the dissimilarity between camera NDVI and camera g_{CC}, highlights the potential for camera NDVI to provide different information about the state of the canopy than can be obtained using only visible-wavelength (RGB) imagery. Furthermore, indices such as EVI (the enhanced vegetation index, which also uses blue channel information) can be calculated from the camera imagery in a similar manner. The resulting data should therefore be of great value for "apples-to-apples" evaluation of landscape phenology products derived from satellite remote sensing, as suitable data for this kind of analysis are currently lacking (cf. Hufkens et al., 2012; note that landscape heterogeneity and the mismatch between the camera field of view and the satellite pixel to which it is being compared remain outstanding challenges). More generally, camera NDVI could be used for continuous monitoring of plant stress in greenhouse or nursery applications, or even quantifying responses to experimental manipulations in large field experiments (e.g. nutrient additions, elevated CO_2, rainfall exclusion, etc.).

Acknowledgments

This work was supported by the National Science Foundation's Macrosystems Biology program (award EF-1065029). We acknowledge additional support from the US National Park Service Inventory and Monitoring Program and the USA National Phenology Network, through a grant from the United States Geological Survey (award G10AP00129). Research at Harvard Forest is partially supported by the National Science Foundation's LTER program (awards DEB-0080592, DEB-1237491). The contents of this paper are solely the responsibility of the authors and do not necessarily represent the official views of NSF or USGS.

References

Betancourt JL, Schwartz MD, Breshears DD, Cayan DR, Dettinger MD, Inouye DW, Post E, Reed BC. 2005. Implementing a U.S. National Phenology Network. *Eos, Transactions American Geophysical Union* **86**: 539.

Garrity SR, Vierling LA, Bickford K. 2010. A simple filtered photodiode instrument for continuous measurement of narrowband NDVI and PRI over vegetated canopies. *Agricultural and Forest Meteorology* **150**: 489-496.

Higgins SI, Delgado-Cartay MD, February EC, Combrink HJ. 2011. Is there a temporal niche separation in the leaf phenology of savanna trees and grasses? *Journal of Biogeography* **38**: 2165-2175.

Huemmrich KF, Black TA, Jarvis PG, McCaughey JH, Hall FG. 1999. High temporal resolution NDVI phenology from micrometeorological radiation sensors. *Journal of Geophysical Research-Atmospheres* **104**: 27935-27944.

Hufkens K, Friedl M, Sonnentag O, Braswell BH, Milliman T, Richardson AD. 2012. Linking near-surface and satellite remote sensing measurements of deciduous broadleaf forest phenology. *Remote Sensing of Environment* **117**: 307-321.

Jenkins JP, Richardson AD, Braswell BH, Ollinger SV, Hollinger DY, Smith ML. 2007. Refining light-use efficiency calculations for a deciduous forest canopy using simultaneous tower-based carbon flux and radiometric measurements. *Agricultural and Forest Meteorology* **143**: 64-79.

Keenan TF, Darby B, Felts E, Sonnentag O, Friedl M, Hufkens K, O'Keefe J, Klosterman S, Munger JW, Toomey M, Richardson AD. 2013. Tracking forest phenology and seasonal physiology using digital repeat photography: a critical assessment. *Ecological Applications* **in review**.

Migliavacca M, Sonnentag O, Keenan TF, Cescatti A, O'Keefe J, Richardson AD. 2012. On the uncertainty of phenological responses to climate change, and implications for a terrestrial biosphere model. *Biogeosciences* **9**: 2063-2083.

Morisette JT, Richardson AD, Knapp AK, Fisher JI, Graham EA, Abatzoglou J, Wilson BE, Breshears DD, Henebry GM, Hanes JM, Liang L. 2009. Tracking the rhythm of the seasons in the face of global change: phenological research in the 21st century. *Frontiers in Ecology and the Environment* **7**: 253-260.

Nijland W, de Jong R, de Jong SM, Wulder MA, Bater CW, Coops NC. 2013. Monitoring plant condition and phenology using infrared sensitive consumer grade digital cameras. *Agricultural and Forest Meteorology* **184**: 98-106.

Polgar CA, Primack RB. 2011. Leaf-out phenology of temperate woody plants: from trees to ecosystems. *New Phytologist* **191**: 926-941.

Richardson AD, Anderson RS, Arain MA, Barr AG, Bohrer G, Chen G, Chen JM, Ciais P, Davis KJ, Desai AR, Dietze MC, Dragoni D, Garrity SR, Gough CM, Grant R, Hollinger DY, Margolis HA, McCaughey H, Migliavacca M, Monson RK, Munger JW, Poulter B, Raczka BM, Ricciuto DM, Sahoo AK, Schaefer K, Tian H, Vargas R, Verbeeck H, Xiao J, Xue Y. 2012. Terrestrial biosphere models need better representation of vegetation phenology: results from the North American Carbon Program Site Synthesis. *Global Change Biology* **18**: 566-584.

Richardson AD, Braswell BH, Hollinger DY, Jenkins JP, Ollinger SV. 2009. Near-surface remote sensing of spatial and temporal variation in canopy phenology. *Ecological Applications* **19**: 1417-1428.

Richardson AD, Jenkins JP, Braswell BH, Hollinger DY, Ollinger SV, Smith ML. 2007. Use of digital webcam images to track spring green-up in a deciduous broadleaf forest. *Oecologia* **152**: 323-334.

Richardson AD, Keenan TF, Migliavacca M, Ryu Y, Sonnentag O, Toomey M. 2013a. Climate change, phenology, and phenological control of vegetation feedbacks to the climate system. *Agricultural and Forest Meteorology* **169**: 156-173.

Richardson AD, Klosterman S, Toomey M 2013b. Chapter 22: Near-surface sensor-derived phenology. In: Schwartz MD ed. *Phenology: An Integrative Environmental Science (2nd Edition)*. New York: Springer, 413-430.

Rosenzweig C, Casassa G, Karoly DJ, Imeson A, Liu C, Menzel A, Rawlins S, Root TL, Seguin B, Tryjanowski P 2007. Assessment of observed changes and responses in natural and managed systems. In: Parry ML, Canziani OF, Palutikof JP, van der Linden PJ, Hanson CE eds. *Climate Change 2007: Impacts, Adaptation and Vulnerability. Contribution of Working Group II to the Fourth Assessment Report of the Intergovernmental Panel on Climate Change*. Cambridge, UK: Cambridge UP, 79-131.

Ryu Y, Baldocchi DD, Verfaillie J, Ma S, Falk M, Ruiz-Mercado I, Hehn T, Sonnentag O. 2010. Testing the performance of a novel spectral reflectance sensor, built with light emitting diodes (LEDs), to monitor ecosystem metabolism, structure and function. *Agricultural and Forest Meteorology* **150**: 1597-1606.

Sakamoto T, Gitelson AA, Nguy-Robertson AL, Arkebauer TJ, Wardlow BD, Suyker AE, Verma SB, Shibayama M. 2012. An alternative method using digital cameras for continuous monitoring of crop status. *Agricultural and Forest Meteorology* **154**: 113-126.

Sakamoto T, Shibayama M, Takada E, Inoue A, Morita K, Takahashi W, Miura S, Kimura A. 2010. Detecting seasonal changes in crop community structure using day and night digital images. *Photogrammetric Engineering and Remote Sensing* **76**: 713-726.

Shibayama M, Sakamoto T, Takada E, Inoue A, Morita K, Takahashi W, Kimura A. 2009. Continuous monitoring of visible and near-infrared band reflectance from a rice paddy for determining nitrogen uptake using digital cameras. *Plant Production Science* **12**: 293-306.

Shibayama M, Sakamoto T, Takada E, Inoue A, Morita K, Takahashi W, Kimura A. 2011. Estimating paddy rice leaf area index with fixed point continuous observation of near infrared reflectance using a calibrated digital camera. *Plant Production Science* **14**: 30-46.

Sonnentag O, Hufkens K, Teshera-Sterne C, Young AM, Friedl M, Braswell BH, Milliman T, O'Keefe J, Richardson AD. 2012. Digital repeat photography for phenological research in forest ecosystems. *Agricultural and Forest Meteorology* **152**: 159-177.

Steltzer H, Welker JM. 2006. Modeling the effect of photosynthetic vegetation properties on the NDVI-LAI relationship. *Ecology* **87**: 2765-2772.

Tucker CJ. 1979. Red and photographic infrared linear combinations for monitoring vegetation. *Remote Sensing of Environment* **8**: 127-150.

Wang Q, Tenhunen J, Dinh NQ, Reichstein M, Vesala T, Keronen P. 2004. Similarities in ground- and satellite-based NDVI time series and their relationship to physiological activity of a Scots pine forest in Finland. *Remote Sensing of Environment* **93**: 225-237.

White MA, de Beurs KM, Didan K, Inouye DW, Richardson AD, Jensen OP, O'Keefe J, Zhang G, Nemani RR, van Leeuwen WJD, Brown JF, de Wit A, Schaepman M, Lin X, Dettinger M, Bailey AS, Kimball J, Schwartz MD, Baldocchi DD, Lee JT,

Lauenroth WK. 2009. Intercomparison, interpretation, and assessment of spring phenology in North America estimated from remote sensing for 1982-2006. *Global Change Biology* **15**: 2335-2359.

Zhang X, Friedl MA, Schaaf CB. 2006. Global vegetation phenology from moderate resolution imaging spectroradiometer (MODIS): Evaluation of global patterns and comparison with in situ measurements. *J. Geophysical Research–Biogeosciences* **111**: Art. No. G04017.

Figure 1. Reflectance spectra of the 51 samples (thin grey lines) used in the laboratory experiment. The heavier black lines indicate representative spectra from a healthy green leaf (bottom), a yellowing leaf (middle), and a red (top) leaf.

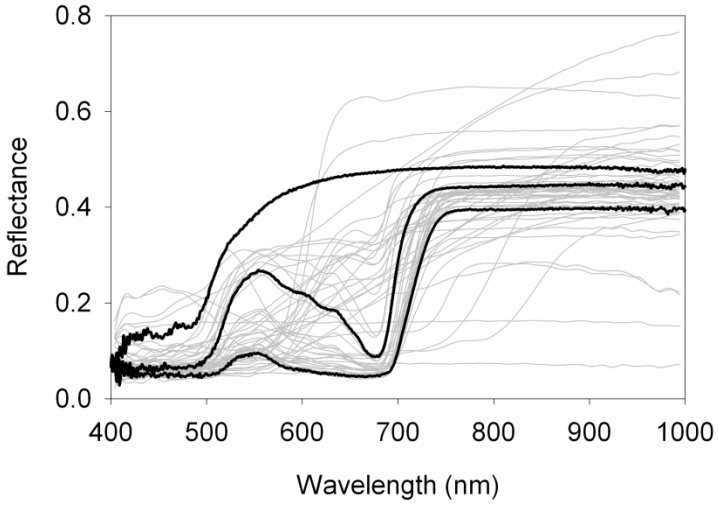


Figure 2. Correlation of digital number (color bands extracted from fixed-exposure camera imagery) and mean reflectance (measured with a spectroradiometer) for $n = 51$ samples in laboratory experiment. (a) mean reflectance from 570-660 nm vs. digital number of camera red channel; (b) mean reflectance from 805-815 nm vs. digital number of NIR component of camera RGB+NIR imagery; (c) spectroradiometer NDVI vs. camera NDVI calculated using R_{DN} and X_{DN}.

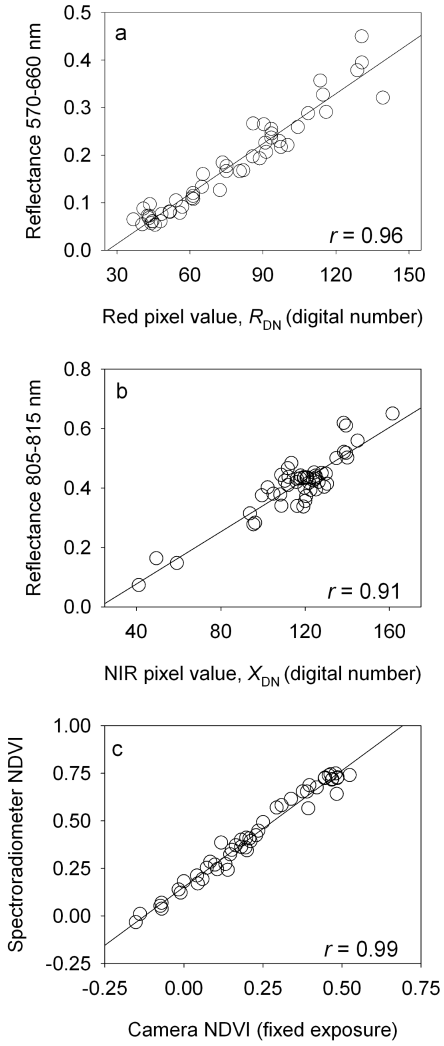


Figure 3. Contour plot showing linear correlation (Pearson's *r*) of pixel values (digital numbers) of individual color bands, from digital camera imagery, with mean spectral reflectance over the region from λ_1 (*x* axis) to λ_2 (*y* axis) nm, as measured on a spectroradiometer. (a) Camera blue channel; (b) camera green channel; (c) camera red channel; (d) NIR component of RGB+NIR imagery.

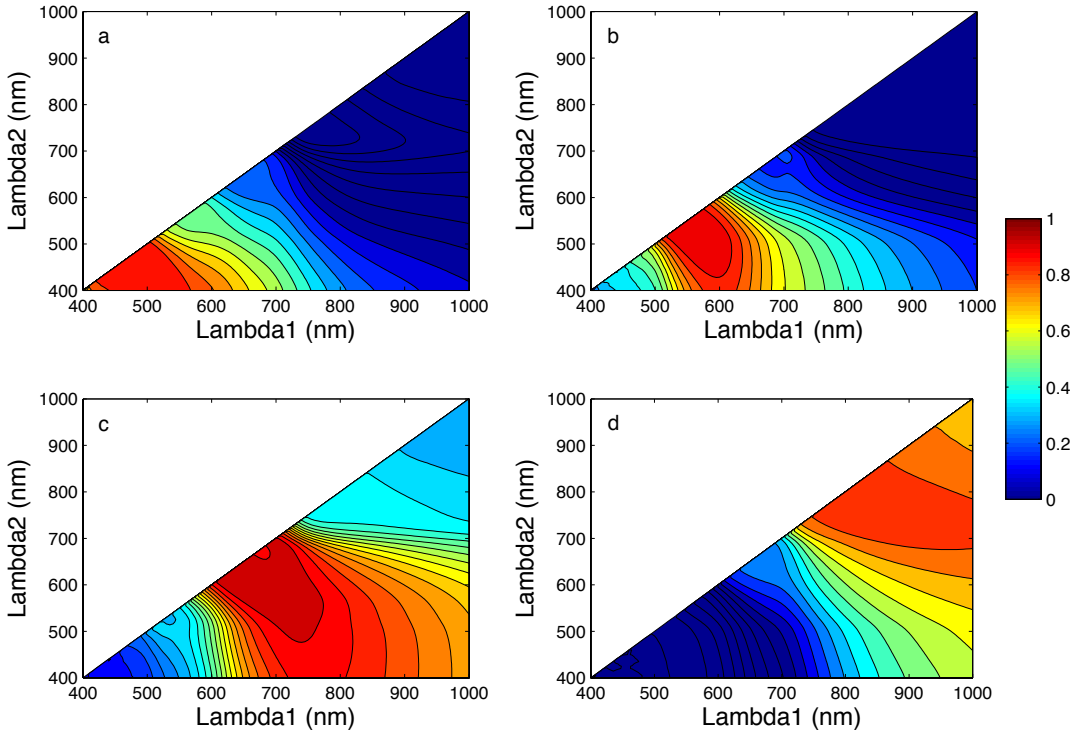


Figure 4. Correlation of exposure-adjusted digital number (color bands extracted from auto-exposure camera imagery) and mean reflectance (measured with a spectroradiometer) for n = 51 samples in laboratory experiment. (a) mean reflectance from 575-710 nm vs. exposure-adjusted digital number of camera red channel (R'_{DN},); (b) mean reflectance from 800-815 nm vs. exposure-adjusted digital number of NIR component of camera RGB+NIR imagery (X'_{DN},); (c) spectroradiometer NDVI vs. camera NDVI calculated using R'_{DN} and X'_{DN} vs. spectroradiometer NDVI.

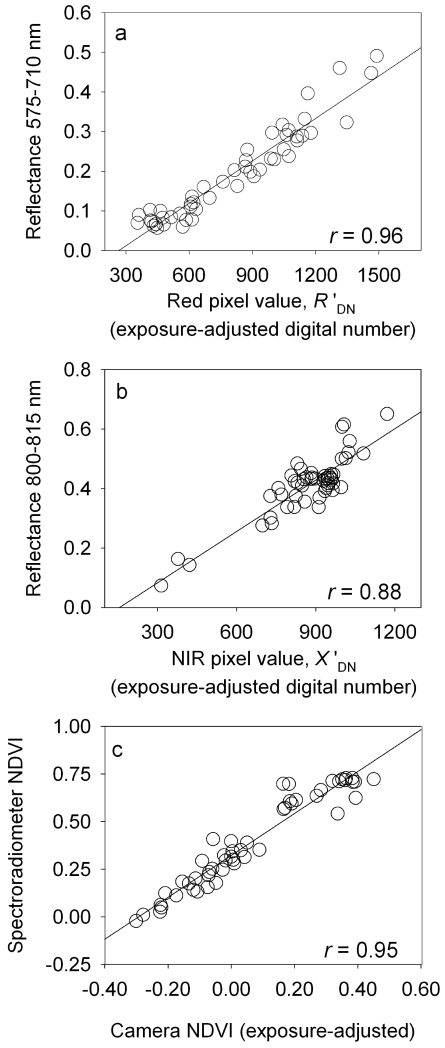


Figure 5. Time series of daily means (calculated for PPFD ≥ 200 μmol m^{-2} s^{-1}) of vegetation indices calculated from radiometric instruments (a, d) and digital camera imagery, analyzed separately for deciduous (b, e) and coniferous (c, f) regions of interest, from instruments mounted on the Harvard Forest Barn Tower. In (d), the gray filled circles are the mean value of MODIS NDVI from a 3x3 window centered on the tower pixel. g_{CC} is the green chromatic coordinate, NDVI is the normalized difference vegetation index.

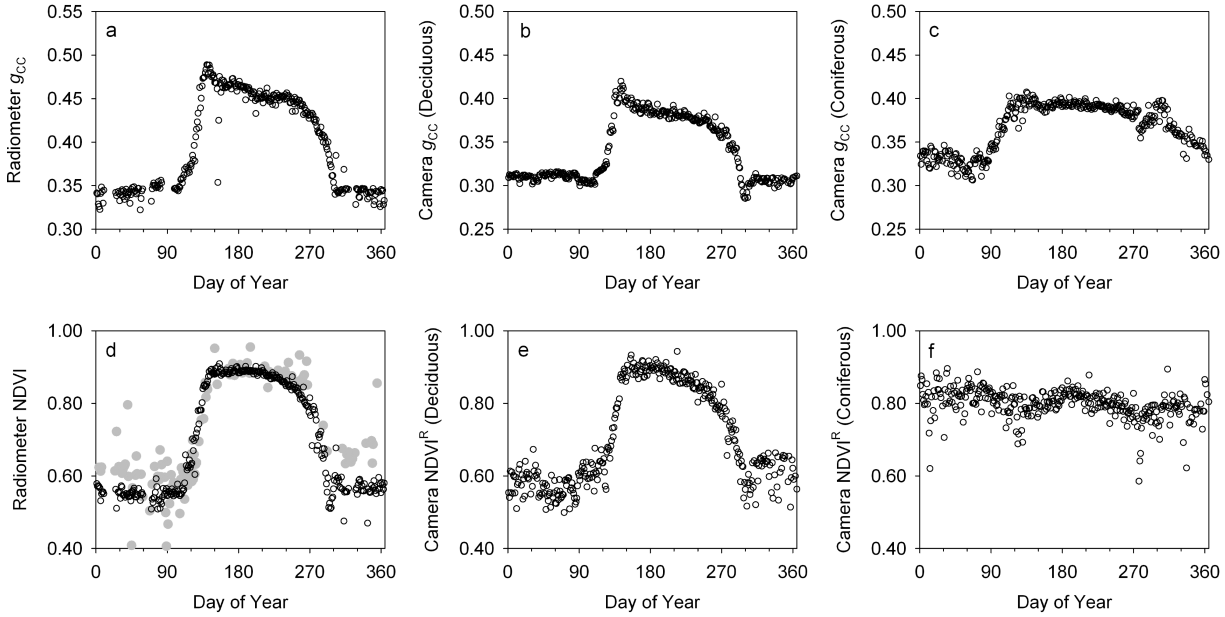


Figure 6. Winter (February 1, top) and summer (July 6, bottom) false-color images (XRG) obtained from an infrared-enabled security camera mounted on the Harvard Forest Barn Tower. The near infrared component (X) is mapped to the red (R) channel, the red channel is mapped to the green (G) channel, and the green channel is mapped to the blue channel. Both images were taken from the top of the tower at 4 PM local standard time. The evergreen trees that are clearly visible in the top image are white pine (*Pinus strobus*).

